A statistical approach for rain intensity differentiation using Meteosat Second Generation-Spinning Enhanced Visible and InfraRed Imager observations

E. Ricciardelli[1], D. Cimini[1], F. Di Paola[1], F. Romano[1], M. Viggiano[1]

[1]{National Research Council of Italy - Institute of Methodologies for Environmental Analysis}

Correspondence to: E. Ricciardelli (elisabetta.ricciardelli@imaa.cnr.it)

Abstract

This study exploits the Meteosat Second Generation (MSG)–Spinning Enhanced Visible and Infrared Imager (SEVIRI) observations to evaluate the rain class at high spatial and temporal resolutions and, to this aim, proposes the Rain Class Evaluation from Infrared and Visible observation (RainCEIV) technique. RainCEIV is composed of two modules: a cloud classification algorithm which individuates and characterizes the cloudy pixels, and a supervised classifier that delineates the rainy areas according to the three rainfall intensity classes, the *non-rainy* (rain rate value<0.5 mm×h^{-1}) class, the *light-to-moderate rainy* class (0.5 mm×h^{-1}≤rain rate value<4 mm×h^{-1}), and the *heavy-to-very-heavy-rainy* class (rain rate value≥4 mm×h^{-1}). The second module considers in input the spectral and textural features of the infrared and visible SEVIRI observations for the cloudy pixels detected by the first module. It also takes the temporal differences of the brightness temperatures linked to the SEVIRI water vapour channels as indicative of the atmospheric instability strongly related to the occurrence of rainfall events.

The rainfall rates used in the training phase are obtained through the Precipitation Estimation at Microwave frequencies, PEMW (an algorithm for rain rate retrievals based on Atmospheric Microwave Sounder Unit (AMSU)-B observations). RainCEIV principal aim is that of supplying preliminary qualitative information on the rainy areas within the Mediterranean basin where there is no radar network coverage. The results of RainCEIV have been validated against radar-derived rainfall measurements from the Italian Operational Weather Radar Network for some case studies limited to the Mediterranean area. The dichotomous assessment related to daytime

(night-time) validation shows that RainCEIV is able to detect rainy/non rainy areas with an accuracy of about 97% (96%), and when all the rainy classes are considered, it shows a Heidke skill score of 67% (62%), a Bias score of 1.36 (1.58), and a Probability of Detection of rainy areas of 81% (81%).

1. Introduction

A wealth of techniques based on geostationary satellite IR/VIS observations have been developed in order to estimate rain rate (RR) values or confidences. A recent overview is given by Kidd and Levizzani (2011). The geostationary satellite techniques perform better over areas where rainfall originates from deep convection than in the areas where it originates from the stratiform systems. In particular, Negri and Adler (1981) examined the relation between cloud top temperature and RR by analysing Geostationary Operational Environmental Satellite (GOES) and radar data associated to a series of thunderstorms. Adler et al. (1985) proposed a Thunderstorm Index (TI) to give probability to observe heavy precipitation. Successively, Adler et al. (1988) extended their interest to stratiform precipitation (produced under the anvils of mature and decaying convective systems) from GOES satellite infrared data. Wu and Weinman (1985) used GOES data in order to estimate rainfall by means of a pattern recognition algorithm trained and tested on different sets of RR measurements obtained from NOAA operational radars. They classify rain into three classes (non-rainy, light rainy, heavy rainy classes). Adler et al. (1993) were the first to successfully combine the advantages of both types of instrument by using matched MW and IR data. Vicente et al. (1998) introduced the auto-estimator in order to estimate rainfall from GOES measurements focusing on heavy precipitation. The auto-estimator differs from the previous IR methods for rainfall estimation because it considers other factors in addition to the IR window cloud top temperature. In particular, information about environmental moisture is used to obtain a more correct estimation of rainfall as well as for the screening of the non-rainy pixels. Ba and Gruber (2001) used the GOES visible (0.65μm), near infrared (3.9 μm), water vapour (6.7μm) and window channels (10.7μm and 12.0 μm) to estimate rainfall rate, distinguishing raining from non-raining clouds by taking into account the cloud top temperature, the effective radius of cloud particles and the temperature gradient. Moreover, in an attempt to give more reliable values of rain rates, Ba and Gruber (2001) used the moisture factor correction

developed by Scofield (1987) and modified by Vicente et al. (1998). Other authors used artificial neural networks to derive precipitation estimates using satellite IR images (Hsu et al., 1997; Behrangi et al., 2009; Capacci and Porcù, 2009). Many authors developed techniques to determine RR from Meteosat data, both physical and statistical. Physical techniques consist of brightness temperature difference threshold tests or consider effective radius as well as cloud top height/temperature in order to determine rainfall rate and/or probability by the use of look-up tables. The look-up tables are usually built by considering rainfall measurements obtained through rain-gauge instruments or radar as well as RR values determined by MW data. An example of IR method that uses RR values determined by MW observations was developed by Jobard and Desbois (1994), the RAin and Cloud Classification method (RACC), that used the SSM/I and Meteosat data in order to classify the Meteosat images into several categories of rain. Turk et al. (2000) proposed a blended geostationary-microwave technique for the retrieval of RR measurements. This technique has been taken as a role model by several investigators (Kidd et al., 2003; Marzano et al., 2004), including Heinemann et al. (2002) who developed the Multi-Sensor Precipitation Estimate (MPE) technique operating at the European agency for the deployment of meteorological satellites (EUMETSAT). MPE product consists of the near-real-time RR maps for each Meteosat Second Generation (MSG)- Spinning Enhanced Visible and Infrared Imager (SEVIRI) images in original pixel resolution. Moreover, recently Mugnai et al. (2013) implemented the blended technique by Turk et al. (2000) among the precipitation products of the Satellite Application Facility on Support to Operational Hydrology and Water Management (H-SAF) H-SAF. Roebeling and Holleman (2009) proposed an algorithm for the RR estimation from the cloud physical properties (such as cloud condensed water path and cloud top height) retrieved from SEVIRI observations. Kuhnlein et al. (2010) also investigated the SEVIRI potential to determine RR, assuming a relationship between RR and optical thickness as well as effective radius. In particular they have established a relation between the reflectance observations acquired at 0.6μm and 1.6μm – which give information about cloud optical thickness and effective radius - and the ground-based rainfall rate. Recently, Feidas and Giannakos (2012) have proposed an algorithm that works with SEVIRI observations by combining physical and statistical methods to characterize convective and stratiform precipitation areas. They calibrated the algorithm using RR measurements derived from a substantial number of rain gauge stations in Greece. Other techniques are based on cloud motion

and exploit IR observations to provide an estimate of cloud movement to be used for transporting the more direct MW rainfall observations (Joyce et al., 2004). Di Paola et al. (2012) proposed the Precipitation Evolving Technique (PET) for convective rain cell continuous monitoring. PET propagates forward in space and time the latest RR map inferred by AMSU and MHS MW observations by using SEVIRI IR brightness temperature maps. This technique is able to propagate the latest rain field available for 2-3 hours. The aim of this study is to propose a technique based on a statistical classification algorithm that uses the spectral and textural features of SEVIRI IR/VIS observations to classify the cloudy pixels as *non-rainy*, *light-to-moderate-rainy*, or *heavy-to-very-heavy-rainy*. The technique proposed, the Rain Class Evaluation from Infrared and Visible observations (RainCEIV), operates in a fixed area, the Mediterranean basin, approximately between 35 and 50 degrees North, and 20 degrees West and 20 degrees East. RainCEIV firstly discriminates cloudy from non-cloudy pixels, then it determines the rain class only for the pixels classified as cloudy. It deploys the k-Nearest Neighbour Mean classifier (k-NNM) which considers as input the spectral and textural features derived from the SEVIRI VIS/IR images and the brightness temperatures differences of SEVIRI water vapour channels acquired 15, 30, and 45 minutes before the time of interest. RainCEIV has been validated against the radar-derived RR values obtained from the Italian *Operational Weather Radar Network* observations managed by the Italian Department of Civil Protection (DPC). RainCEIV is proposed as a useful tool to achieve a real-time monitoring of rainfall events, both the intense convective and the stratiform moderate ones.

Section 2 provides a description of the satellite sensors whose observations and/or products have been used for the RainCEIV implementation; Section. 3 describes the two modules of RainCEIV (the C_MACSP cloud classification algorithm and the RainCEIV k-NNM classifier); Section 4 shows the statistical scores obtained by comparing RainCEIV and radar-derived RR measurements.

2. Instruments and data description

The spectral and textural features of MSG-SEVIRI images are used as input for both the C_MACSP cloud classification algorithm and the RainCEIV k-NNM classifier. SEVIRI is the main payload on board the MSG series, composed by MSG-1 (Meteosat 8), MSG-2 (Meteosat

9), MSG-3 (Meteosat 10), and future MSG-4 (Meteosat 11), planned for launch in 2015. SEVIRI is a 50 cm-diameter-aperture line-by-line scanning radiometer and observes the Earth-atmosphere system in 11 channels at (a) full disk with a 3km spatial sampling at the sub-satellite point. In addition, the High Resolution Visible (HRV) channel covers half the full disk with a 1km spatial sampling at the sub-satellite point. The actual instantaneous field of view is about 4.8 km at the sub-satellite point for all the channels except for the HRV channel where it is 1.67 km. The major improvements with respect to previous sensors are its enhanced spectral characteristics, its higher temporal resolution (15 min), the improved signal-to-noise ratio, and the higher precision of data storing which ranges from 8 bits (256 levels) on Meteosat-7 to 10 bits (1024 levels) on Meteosat-8 (Schmetz et al., 2002).

The RainCEIV k-NNM classifier has been trained on the RR product from the Precipitation Estimation at Microwave Frequencies (PEMW). PEMW was developed by Di Tomaso et al. (2009) at the Institute of Methodologies for Environmental Analysis of the National Research Council of Italy (IMAA-CNR) to infer surface rain intensity from satellite MW LEO observations provided by the Advanced Microwave Sounding Unit-B (AMSU-B) and the Microwave Humidity Sounder (MHS) on board the National Oceanic and Atmospheric Administration (NOAA) satellites and the European Polar Satellite MetOp-A, respectively. AMSU-B and MHS are cross-track, line-scanning MW radiometers which measure radiances in five channels in the 89GHz-to-190GHz frequency range. The centre frequencies for the two window channels are 89 GHz, 150 GHz, while the three opaque (water vapour) channels are centred at 183±1, 183±3, and 183±7 GHz. The AMSU-B and MHS fields of view (FOV) have a circular shape (with a diameter of about 16 km) at nadir, while their shape become ellipsoidal away from the nadir (the axes length is 51 km for the cross-track direction and 25 km for the along-track direction at the maximum scanning angle) (Bennartz, 2000). The purpose of these instruments is to measure the radiation from different layers of the atmosphere in order to obtain global data on humidity profiles. The PEMW RR value is assigned to the SEVIRI pixel only when the latter is entirely enclosed in the corresponding AMSU-B/MHS FOV. PEMW RR values are re-sampled on the SEVIRI grid by calculating the area of each AMSU-B/MHS FOV on the basis of the orbital parameters described in (Bennartz, 2000). The temporal matching is carried out considering a maximum difference of 7.5 minutes between the acquisition time of the SEVIRI pixel and that of the AMSU/MHS FOV. For simplicity, the SEVIRI pixel, to which the

PEMW-RR value is assigned, will be denominated PEMWinSEVIRI while the corresponding PEMW-RR value will be denominated PEMWinSEVIRIv.

The RainCEIV results have been validated on the basis of the RR values derived from the Italian Weather Radar Network which is coordinated by DPC (Vulpiani et al., 2008) in collaboration with the regional authorities, the research centres, the Air Traffic Control service (ENAV), and the Meteorological Service of the Italian Air Force (CNMCA). It consists of twenty microwave weather radars belonging to the regional authorities (ten C-band radars), ENAV (two C-band radars) and DPC (six C-band radars and two X-band polarimetric radars). The surface rate intensity (sri, in $mmxh^{-1}$) and other products such as the Vertical Maximum Intensity (VMI), the Constant Altitude Plan Position Indicator (CAPPI) and the one-hour-accumulated surface rain total (srt, in mm), are retrieved from measured reflectivity volumes. Procedures for mitigating ground clutter, an anomalous propagation, beam blockage effects are applied (Vulpiani et al., 2008). The sri product is derived applying a reflectivity-rainfall (Z-R) relationship to the Lowest Beam Map (LBM), i.e. the reflectivity values at the lowest level of the corrected radar volumes. The sri product used here represents the best estimate from the radar network available for the period under analysis, and it has already been used to validate satellite rainfall estimates (Cimini et al., 2013), including EUMETSAT H-SAF products (Puca et al., 2014). Procedures to improve the quality of the sri product, including attenuation compensation, polarimetric rainfall inversion techniques, and adaptive algorithms to retrieve the mean vertical profiles of reflectivity have recently been developed at DPC (Vulpiani et al., 2012; Rinollo et al., 2013). All the products are available on a grid of 1400x1400 km^2 with a spatial resolution of circa 1 km and a temporal resolution of 15 minutes. For simplicity, the radar samples completely included into the SEVIRI pixels will be denominated RS samples. The collocation process of the radar-derived RR measurements into the SEVIRI grid consists in associating the RS samples to each SEVIRI pixel. If the percentage of the rainy RS samples is higher than 80%, the SEVIRI pixel is considered for the validation and classified as *light-to-moderate-rainy* or *heavy-to-very-heavy-rainy* on the basis of the RS-RR value average. In some cases, the RS-RR value average is strongly influenced by the lowest RR values of the *light-to-moderate-rainy* RS samples also if the number of *heavy-to-very-heavy rainy* RS samples is higher than that of the *light-to-moderate-rainy* one. Because of this, when the percentage of the *heavy-to-very-heavy-rainy* RS samples is higher than 50% and it is higher than that of the *light-to-moderate-rainy* RS samples, the SEVIRI pixel is flagged as

heavy-to-very-heavy-rainy regardless of the RS-RR value average. If the percentage of the non-rainy RS samples is 100%, the SEVIRI pixel is considered for the training and validation. In the other cases, the SEVIRI pixel is flagged as "uncertain" and not considered for the training and validation purposes. For simplicity, the pixel SEVIRI, to which the radar-derived-RR value is assigned, will be denominated RADARinSEVIRI, while the corresponding RR value will be denominated RADARinSEVIRIv.

3. RainCEIV description

The RainCEIV technique consists of two modules:

I- a cloud classification algorithm that discriminates *clear* from *cloudy* pixels and further classifies the cloudy pixels;

II- a k-Nearest Neighbour Mean (k-NNM) classifier that evaluates the rain class for each pixel classified as cloudy by the first module.

3.1 Cloud classification algorithm description

The cloud Mask Coupling of Statistical and Physical methods algorithm - MACSP (Ricciardelli et al., 2008; Di Paola et al., 2014) - is used for distinguishing *cloudy* from *non-cloudy* pixels. The version used for RainCEIV purposes is called C_MACSP, which stands for cloud Classification Mask Coupling of Statistical and Physical methods. The current version has been updated to give information about the cloud class and in particular to split the MACSP "*high cloud*" in the "*high optically thin"* and "*high optically thick*" cloud classes. Furthermore, the *convective cloud* class has been added, not just for module II but also to individuate the possible occurrence of extreme events. A pixel can be classified in 5 different classes considered both over land and sea: *clear*, *low*/*middle cloud*, *high optically thin cloud*, *high optically thick cloud* and *convective cloud*. In detail, the C_MACSP physical algorithm uses the same physical threshold tests as the MACSP earlier version with the addition of a new threshold test involving the difference between the brightness temperature of the SEVIRI water vapour channel centred at 6.2μm and of the SEVIRI window channel centred at 10.8μm, $\Delta TB_{6.2\mu m-10.8\mu m}$. This difference is very small for convective cloud as asserted by Mosher (2001, 2002) in the Global Convective Diagnostic approach. The C_MACSP statistical (temporal) algorithm considers in input the same spectral

and textural features described and listed in section 3.2.1 (section 3.4) and Table 4 (Table 7), respectively, of Ricciardelli et al. (2008), but the training dataset has been updated in order to build the training samples for the *convective cloud* class. The training samples were collected in the Mediterranean basin, where RainCEIV operates. The cloud classification for the training dataset has been made through a careful visual inspection of the SEVIRI images. The clear and cloudy pixels have been selected manually after observing the spectral characteristics in SEVIRI IR/VIS images as well as in their RGB composition, a useful practice for distinguishing cloudy classes (Lensky and Rosenfeld, 2008). In order to collect the training samples for the *convective cloud* class, the cloudy SEVIRI pixels have been matched with the corresponding PEMW-RR and radar-derived RR values, if available. The collocation process both of the radar-derived RR values and the PEMW-RR values in the SEVIRI grid is described in Section 2. The SEVIRI pixel is considered for the training when:

- both the RADARinSEVIRI pixel and PEMWinSEVIRI pixel are available and the relation:
  (RADARinSEVIRIv$\geq$4mm$\times$h^{-1}).and.(PEMWinSEVIRIv$\geq$4mm$\times$h^{-1}) is satisfied;
- both the RADARinSEVIRI pixel and PEMWinSEVIRI pixel are available and the relation:
  (RADARinSEVIRIv$\geq$4mm$\times$h^{-1}).and.(PEMWinSEVIRIv<4mm$\times$h^{-1}) is satisfied and the percentage of the rainy RS samples is higher than 80%;
- only the PEMWinSEVIRI pixel is available (the AMSU-B/MHS observation is outside the area covered by the Radar Network) and the relation (PEMWinSEVIRIv$\geq$4mm$\times$h^{-1}) is satisfied.

When both the RADARinSEVIRI pixel and the PEMWinSEVIRI pixel are available and the relations at points 2 and 3 are not satisfied, the SEVIRI pixel is not considered for the initial training dataset. The SEVIRI images listed in table 5 of Ricciardelli et al (2008) and in particular the ones used for the training of the Mediterranean basin (enclosed in the areas B, C, and G of Figure 3 of Ricciardelli et al (2008)) have been used for the training of C_MACSP. The SEVIRI images used for the training are those acquired on 29 September 2009 at 16:57 UTC, on 1 October 2009 (at 05:12 UTC, at 08:27 UTC, and at 15:57 UTC), on 04 March 2010 (at 14:27 UTC, 15:57 UTC, and at 20:12 UTC), on 28 April 2010 (at 12:27 UTC and 15:43 UTC), on 4

August 2010 (at 10:43 UTC and 15:12 UTC), on 2 February 2010 at 22:57 UTC, on 8 January 2010 at 13:57 UTC, on 1 October 2009 at 05:13 UTC and 19:13 UTC. The procedure described in Appendix A has been applied in order to refine the training dataset by eliminating the redundant as well as the misclassified samples. The C_MACSP statistical and physical algorithms are applied separately to each SEVIRI pixel, and the results are compared. If they agree, the SEVIRI pixel is classified consequently, otherwise the temporal algorithm is applied in order to remove the ambiguity and classify the SEVIRI pixel definitively. For RainCEIV purposes, the C_MACSP screening is useful to:

- reduce the number of the input pixels to the RainCEIV k-NNM classifier by removing the pixels classified as *clear* and *high thin cloud*;
- define the components of the feature vector in input to the RainCEIV classifier (as will be described in the following sub-section. The components chosen for each cloud class are shown in Tables 5 and 6).

3.2 k- Nearest Neighbour Mean classifier description

The classifier pattern used to evaluate the rainy class is the k-Nearest Neighbour Mean (k-NNM) non-parametric supervised classifier proposed by Viswanath and Sarma (2011). This classifier has been chosen for its simplicity and good performance (Dasarathy, 1991; Dasarathy 2002; Babu and Viswanath, 2009) and because, unlike the Bayes classifier, it does not assume any *a priori* known probabilities, which are estimated directly from the design samples. It implements the decision rule locally. The k-NNM classifier has demonstrated to perform better than the k-NN classifier and it is suitable for parallel implementation so as to reduce the classification time, as asserted by Viswanath and Sarma (2011).

Let $\vec{x}$ be the vector of features related to the pixel to be classified and C_i the *rainy/non-rainy* class with i=0,1,2 defined as follows:

1. *non-rainy* class (RR<0.5mm×h^{-1}) (C_0)
2. *light-to-moderate rainy* class (0.5≤RR≤4mm×h^{-1}) (C_1)
3. *heavy-to-very-heavy rainy* class (RR>4mm×h^{-1}) (C_2)

For each class C_i the k-NNM classifier finds the k (where $k \geq 1$) nearest neighbours of $\vec{\mathbf{x}}$ and determines the mean value $d_{mean}(\vec{\mathbf{x}}, C_i)$ of their distances ($d(\vec{\mathbf{x}}, \vec{\mathbf{x}}_{\mathbf{i,j}})$) from $\vec{\mathbf{x}}$.

$$d_{mean}(\vec{\mathbf{x}}, C_i) = \frac{\sum_{j=1}^{k} d(\vec{\mathbf{x}}, \vec{\mathbf{x}}_{\mathbf{i,j}})}{k} \qquad \text{i=0,1,2} \qquad (1)$$

where $d(\vec{\mathbf{x}}, \vec{\mathbf{x}}_{i,j})$ is the Euclidean distance between $\vec{\mathbf{x}}$ and $\vec{\mathbf{x}}_{\mathbf{i,j}}$ which is the j^{th} nearest training sample for the class C_i. The pixel is labelled as the class characterized by the lowest mean distance $d_{mean}(\vec{x}, C_i)$:

- $(d_{mean}(\vec{x}, C_0) < d_{mean}(\vec{\mathbf{x}}, C_1)) and (d_{mean}(\vec{\mathbf{x}}, C_0) < d_{mean}(\vec{\mathbf{x}}, C_2)) \rightarrow \vec{\mathbf{x}} \in C_0$ (2)
- $(d_{mean}(\vec{\mathbf{x}}, C_1) < d_{mean}(\vec{\mathbf{x}}, C_0)) and (d_{mean}(\vec{\mathbf{x}}, C_1) < d_{mean}(\vec{\mathbf{x}}, C_2)) \rightarrow \vec{\mathbf{x}} \in C_1$ (3)
- $(d_{mean}(\vec{\mathbf{x}}, C_2) < d_{mean}(\vec{\mathbf{x}}, C_0)) and (d_{mean}(\vec{\mathbf{x}}, C_2) < d_{mean}(\vec{\mathbf{x}}, C_1)) \rightarrow \vec{\mathbf{x}} \in C_2$ (4)

Fig. 1 shows the scheme of the RainCEIV technique.

3.2.1 Features selection and description

The k-NNM classifier uses textural and spectral features estimated in 3×3-pixel boxes in order to associate each SEVIRI pixel to a rainy/non-rainy class. The textural and spectral features used in this study and their different weights in the grid element, where both textural and tonal features have significant values, are described in Ricciardelli et al. (2008). In detail, the spectral features used are the *maximum* and *minimum* grey levels and the ratio between them. The textural features considered are the *maximum* and the *minimum* of the Entropy (a measure of the spatial randomness of the image), the Angular Second Moment (ASM, a measure of homogeneity of the image), the Contrast (a measure of local variation of the grey-level differences) and the Mean (a measure of the mean grey-level differences). The maximum and minimum values are calculated among the values calculated for the four directions (0º, 45º, 90º, 135º) in the 3×3-pixel box. All the spectral and textural features defined for the IR/VIS SEVIRI images acquired at 0.6 µm, 0.8 µm, 1.6 µm, 3.9 µm, 6.2 µm, 7.3 µm, 10.8 µm, and 12µm were initially considered as components of $\vec{\mathbf{x}}$. Some of the above-listed spectral channels are usually utilized to infer information on cloud-top microphysical properties. In particular, the observations acquired at 10.8 µm and 12.0 µm are used to provide information on cloud top temperature and cloud optical thickness, the observations at 0.6 µm are also used to get information about cloud optical thickness, while the 3.9 µm and 1.6 µm observations are used to infer information on the cloud thermodynamic phase and cloud effective radius. The precipitation processes are strongly related to the cloud-top microphysical structure and, in particular, the rain rate confidence is high for

cloud tops with large cloud droplets or in the presence of ice (Lensky and Rosenfeld, 1997). Consequently, in this study the use of features derived from spectral channels connected with cloud microphysical properties could allow the identification of raining clouds.

The spectral channels centred at 6.2 μm and 7.3 μm are indicative of the water vapour (WV) content in the troposphere at pressure levels lower than 400hPa and 600hPa, respectively. The WV channel features when considered alone do not give useful information on the presence of a raining cloud, on the contrary, when considered with the other channel features, in particular those related to the 10.8 μm channel, they are useful to individuate convective events (Mosher, 2001, 2002). Moreover, the WV temporal changes are indicative of the atmospheric instability that is a useful index in the detection of the precipitating area. Because of this, the temporal differences $\Delta TB_{(6.2)15-30}$, $\Delta TB_{(6.2),15-45}$, $\Delta TB_{(6.2),30-45}$, $\Delta TB_{(7.3)15-30}$, $TB_{(7.3),15-45}$, $TB_{(7.3),30-45}$ between the WV brightness temperatures related to the SEVIRI acquisitions made 15, 30 and 45 minutes before the time of interest are exploited to get information on the WV temporal changes at different atmosphere levels. Obviously, the temporal change of WV brightness temperature related to a pixel does not always mean that the pixel is rainy, and as for the other features, it gains usefulness in discriminating rainy/non-rainy classes when used in combination with the other features opportunely chosen, as will be described in the following sub-section.

Before defining and listing the final components of the feature vector, it is important to explain how these features have been normalized so as to prevent the features (x^i) characterized by the largest variance across the training data set from dominating the Euclidean distance. The normalization formula applied to each feature is:

$$\tilde{x}^i = \frac{x^i - \bar{x}^i}{\sigma^i} \quad (5)$$

where x^i is the i^{th} component of the feature vector $\vec{\mathbf{x}}$ to be normalized, $\tilde{x}^i$ is the ith component of the normalized $\vec{\tilde{\mathbf{x}}}$, $\bar{x}^i$ and σ^i are, respectively, the mean and the standard deviation for the feature x^i calculated considering all the training set samples. This equation is also applied to the feature vector related to the pixels to be classified.

By bearing in mind that the k-NNM classifier performance generally decreases with the dimension of the feature vector, the number of the feature vector components (x^i) has been

reduced. For this purpose, the Fisher distance criterion (Ebert, 1987; Parikh, 1977), described in Appendix A, has been applied in order to evaluate the discriminatory power of the individual features. The Fisher distance has been determined for the following combinations: (C_0, C_1); (C_0, C_2); (C_1, C_2). The features have been ordered in a descending way on the basis of the correspondent Fisher distance value, so that the features characterized by higher Fisher distances have been chosen as components of the feature vector. The definitive values of the feature vector components *d* and the RainCEIV k-NNM classifier *k* parameter have been determined as described in the following sub-section.

3.2.2 Training procedure

The training dataset has been built by collecting a set of SEVIRI images during day- and night-time with collocated RR values inferred from AMSU-B/MHS observations processed with the PEMW algorithm (Di Tomaso et al., 2009), both over land and sea. PEMW exploits the window and water vapour channel observations.. PEMW estimates show a very good agreement with ground-based observations in the detection of rainfall and a reasonably good estimation of RR values. The Probability of Detection (POD) of precipitation is 75% and 90% for RR greater than $1mm \times h^{-1}$ and $5mm \times h^{-1}$, respectively (Di Tomaso et al., 2009). At present, the PEMW algorithm operative version (OPEMW) is operationally run 24/7 at IMAA-CNR. OPEMW has been validated by Cimini et al. (2013) against radar-derived RR values and rain gauge surface rain intensity. The analysis shows an accuracy of 98% in identifying rainy and non-rainy areas and a Heidke skill score of 45% (with respect to radar-derived RR values) and 42% (with respect to rain gauge RR values). The *accuracy*, *Bias Score*, *Probability of Detection*, *False Alarm Ratio* (FAR), *Heidke Skill Score* (HSS) are described in Ebert (2013). The AMSU-B/MHS observations used for building the training database are collected during the NOAA satellite passes over the Mediterranean area on the dates listed in Table 1.

The training dataset has been built by coupling cloudy SEVIRI pixels with the corresponding RR value calculated by the PEMW algorithm and, where available, with the radar-derived RR values. When no radar-derived RR value is available (because the AMSU-B/MHS observation is outside the area covered by the Radar Network) the SEVIRI pixel is classified as belonging to one of the classes C_0, C_1, and C_2 on the basis of the corresponding PEMWinSEVIRIv and it is included in the initial training dataset. When the RADARinSEVIRIv is available and agrees with

the PEMWinSEVIRIv in determining the rainy/non-rainy class the SEVIRI pixel belongs to, this is included in the initial training dataset. Otherwise, when the RADARinSEVIRIv and PEMWinSEVIRIv do not agree, the SEVIRI pixel is included in the initial training dataset only if the correspondent RADARinSEVIRI pixel belongs to a rainy class C_1 or C_2 and the percentage of the rainy RS is higher than 80%. This choice is very useful for the training of the rainy events localized over an area smaller than the AMSU-B/MHS FOV area. The training samples have been considered separately for land and sea and grouped on the basis of the Solar Zenith Angle (SZA). Finally, in order to refine the training dataset, the process described in Appendix A has been applied to the initial training dataset. The availability of the SEVIRI samples double matched with PEMW and radar-derived RR values is useful both for the mitigation of uncertainty due to the collocation process and the refinement of the original training dataset especially for the removal of the misclassified samples. Figure 2 describes the training procedure.

Successively, in order to decide the best values for *d* and *k*, a set of test samples have been classified by varying *d* and *k* combinations. Moreover, an artificial dataset, smoother and more versatile than the initial one, has been obtained by applying the bootstrap method (described by Hamamoto et al. (1997)) to the initial test samples. In order to make a more robust choice for *d* and *k*, the same *d* and *k* combinations chosen for the classification of the initial test dataset have been used to classify the artificial dataset. The best choice of *d* and *k* has been made by comparing the statistical scores obtained by classifying the two dataset separately. Both the initial and the artificial dataset contains the same number of samples for each class.

Let $Y = \{(\vec{y}_i, C_j)\}$ be the independent test dataset built by examining the PEMW-RR values related to the AMSU-B/MSH overpasses of 12 February 2012 at 01:35UTC, 12 November 2011 at 08:50UTC, 22 November 2010 at 09:34 UTC, 4 August 2010 at 14:46 UTC, 26 April 2010 at 12:26 UTC, 01 October 2009 at 19:50UTC, 02 October 2009 at 05:00UTC. The pairs $(\vec{y}_i, C_j)$ indicate the test samples $\vec{y}_i$ belonging to the class C_j, j=1, 2, ..., N_c, N_c is the number of the classes (for RainCEIV C_j, j=0, 1, 2, N_c=3) i=1, 2, ...,$N_{c,j}$, $N_{c,j}$ is the number of the test samples for the class C_j.

The bootstrap samples for each class have been determined as follows:

1. the sample $(\vec{y}_k, C_j)$ was selected;
2. r was chosen equal to $N_{c,j}/4$ and the r Nearest Neighbours (NN) of the sample $(\vec{y}_k, C_j)$ (indicated as $\{(\vec{y}_{k,s}, C_j)_{s=1,r}\}$) were found. (the NN decision rule is explained in Appendix A);
3. the i[th] component of the bootstrap sample was calculated by applying the equation

$$by_k^i = \frac{1}{r} \sum_{s=1}^{r} y_{k,s}^i \quad (7)$$

to all the components of the $\{(\vec{y}_{k,s}, C_j)_{s=1,r}\}$. For simplicity the generic i[th] component of the $(\vec{y}_{k,s}, C_j)_{s=1,r}$ is indicated as $y_{k,s}^i$ without indicating the belonging class C_j, in the same way by_k^i is the i[th] component of the bootstrap sample $(\overrightarrow{by}_k, C_j)$ obtained by starting from the sample $(\vec{y}_k, C_j)$.

4. Points 2 and 3 were repeated for each of the following r values: $r = {}^{N_{c,j}}/_{5}, {}^{N_{c,j}}/_{10}, {}^{N_{c,j}}/_{2} - 8, {}^{N_{c,j}}/_{2} - 6, {}^{Nc,_j}/_{2} - 4, {}^{N_{c,j}}/_{2} - 2;$
5. the process restarted from point 1 with another sample and points 2, 3 and 4 were applied until all the test samples were considered for each class.

A careful screening has been done to eliminate the redundant *bootstrap* samples. The *bootstrap* (artificial) samples and the initial test samples have been classified separately by means of the k-NNM (using the original training dataset). The statistical scores obtained for the two datasets are quite similar and they change in the same way varying *d* and *k* as can be noted in Tables 2, 3 and 4 that list the statistical scores for k=3, d=10, d=16, d=20(Table 2); k=5, d=10, d=16, d=20 (Table 3); k=7; d=10, d=16, d=20 (Table 4). Other combinations of *d* and *k* have been investigated obtaining results worse than the ones listed in tables 2, 3 and 4. In particular, both for the original and artificial test dataset, for $k < 3, d < 10$ the FAR related to the moderate class is higher than 40% and POD is lower than 60%, while for *k*>7 the FAR for all the classes is higher than 44% and the other statistical scores are lower than those obtained for the other *k* and *d* combinations. The statistical scores obtained by classifying the initial and artificial samples agree in suggesting k=5 and d=16 as the best choice of parameters for the k-NNM classifier. The features chosen as components of the feature vector $\vec{\mathbf{x}}$ related to daytime and night-time acquisition are listed in Table 5 and Table 6, respectively. The features used over land and over sea are the same, but in some cases they vary for different cloud classes, e.g. the max value of

the ASM is very useful in order to determine the confidence that a low/middle cloud is precipitating, but its discriminatory power is not so high as to individuate the precipitating high thick clouds. On the contrary, the minimum and maximum values of Entropy, Mean and Contrast give an useful contribution in detecting both *light-to-moderate rainy* class *and heavy-to-very-heavy-rainy* class for all the cloudy classes.

4. Validation results

4.1 C_MACSP validation results

The validity of the C_MACSP algorithm has been tested by applying it to an independent dataset of which each class is made 300 samples taken from the SEVIRI images acquired on 12 November 2010 at 11:27 UTC, 22 November 2010 at 09:27 UTC and at 11:43 UTC, 5 May 2012 at 20:27 UTC, 19 May 2012 at 10:57 UTC, 23 July 2012 at 10:27 UTC, 5 December 2012 at 08:43 UTC, 19 September 2009 at 19:13 UTC, 6 July 2010 at 11:27 UTC and 12:27 UTC, 4 August 2010 at 14:27 UTC, 26 December 2013 at 04:57 UTC, 8 October 2013 at 18:57 UTC, 7 October 2013 at 00:57 UTC and 20 January 2014 at 23:57 UTC. The validation has been carried out separately for samples acquired during night-time and daytime by comparing the C_MACSP classification results and the samples manually collected from the independent dataset images. The manual classification has been made through a careful observation of the SEVIRI RGB composition so as to get the same number of samples for each class. The convective cloud classification results have been validated considering the RR maps derived both from the weather radar network and the PEMW rain rate maps. The latter have been used for the areas where radar information is missing. The accuracy (defined as the ratio between the number of the test samples classified correctly and the total number of the test samples) has been determined for each class and Table 7 shows the results obtained. On the basis of the samples examined, it is possible to assert that C_MACSP is able to classify high thick clouds as well as convective clouds, both over land and sea during daytime and night-time, with an accuracy higher than 95%. Moreover, it shows an accuracy higher than 91% in detecting low/middle clouds both during daytime and night-time over land and over sea. The accuracy in detecting high thin class over sea is 87,6% during daytime and night-time, and it is slight lower over land both during daytime (85%) and night-time (84%).

4.2 RainCEIV validation results

The RainCEIV results have been validated against the RR values derived from the weather radar network operated by the DPC. Table 8 lists the case studies used for validation. Tables 9 and 10 sum up the contingency values for the RainCEIV dichotomous statistical assessment related to the daytime and night-time measurements, respectively. The statistical scores (shown in Table 11) have been calculated for all the classes considered together and for the *light-to-moderate-rainy* (C_1) and the *heavy-to-very-heavy-rainy* (C_2) classes separately. The accuracy scores for all the rainy/non-rainy pixels are 97% and 96% for daytime and night-time, respectively, when all the rainy classes are considered. High values for accuracy scores are related also to the C_1 and C_2 classes considered separately both for daytime and night-time. These results are significantly influenced by the number of the *correct negatives*. The Bias scores indicate the RainCEIV tendency to overestimate the rainy events for all the rainy classes (Bias=1.36 for daytime, Bias=1.58 for night-time) as well as the C_1 (Bias=1.33 for daytime, Bias=1.55 for night-time) and C_2 (Bias=1.65 for daytime, Bias=1.89 for night-time) classes considered separately. FARs, that gives the same information as Bias score without considering the misses, related to all the rainy classes are 39% and 48% for the daytime and night-time validations, respectively. POD, that indicates the ability to detect rainy areas without considering the false alarms, is 81% for all the rainy classes both for night-time and daytime validations. POD indicates the ability of RainCEIV to detect rainy areas with a good approximation, but FAR shows its tendency to overestimate the number of rainy pixels. This tendency of RainCEIV will be analysed more in detail considering the statistical scores related to the C_1 and C_2 classes separately. In order to be clearer it is necessary to give the following definitions:

- the percentage of the C_2inC_1 samples (that are the samples classified as belonging to the C_2 class but that actually belong to the C_1 class) out of the total number of the C_1 samples used for validation will be indicated as %C_2inC_1;
- the percentage of the C_1inC_2 samples (that are the samples classified as belonging to the C_1 class but that actually belong to the C_2 class) out of the total number of the C_2 samples used for validation will be indicated as %C_1inC_2;

- the percentage of the C_2inC_0 samples (that are the samples classified as belonging to the C_2 class but that actually belong to the C_0 class) out of the total number of the C_0 samples used for validation will be indicated as %C_2inC_0;
- the percentage of the C_0inC_1 samples (that are the samples classified as belonging to the C_1 class but that actually belong to the C_0 class) out of the total number of the C_0 samples used for validation will be indicated as %C_0inC_1.

In detail, the Bias score is higher for the C_2 class than for the C_1 one, and this proves the general RainCEIV tendency to overestimate the "*heavy-to-very-heavy-rainy*" pixels. Moreover, FAR/POD related to the C_2 class is 47%/86% and 65%/65% for daytime and night-time validation, respectively. It is worth remarking that the FAR high values are due prevalently to the lower number of the C_2 samples. FAR related to the C_2 class is mainly affected by %C_2inC_1. In fact, %C_2inC_0 (0.2% for daytime and 0.3% for night-time) is lower than %C_2inC_1 (2.4% for daytime and 5.6% for night-time). This means that RainCEIV detects prevalently rainy areas, as testified by the POD value, but tends to misclassify C_1 samples as C_2 samples. In many cases RADARinSEVIRIv related to the misclassified C_1 samples is higher than 3mm×h^{-1}. The FAR/POD score related to the C_1 class is 41%/77% for daytime and 51%/75% for night-time. %C_0inC_1 (2.0% for daytime and 2.8% for night-time) is lower than %C_2inC_1 (11.0% for daytime and 28.2% for night-time).This points out both that RainCEIV is inclined to misclassify the C_2 samples as C_1 samples and the overestimation of the rainy area is mainly due to the misclassification of the non-rainy pixels as belonging to the C_1 class. The POD score related to the night-time validation is quite similar to the POD score related to the daytime validation for all the rainy classes and the C_1 class (81% and 75% respectively), and it is lower for the C_2 class (65%). The worst values of the night-time statistical scores especially for the C_2 class are mainly due to the unavailability of the spectral/textural features related to the VIS/NIR observations, that are characterized by a discriminatory power higher than that related to the spectral/textural features of the 3.9 μm and 12.0 μm observations. HSS has also been considered. It is a measure of the correct forecasts after eliminating those whose correctness would be due exclusively to a random chance. The HSS value obtained for RainCEIV and related to the daytime (night-time) validation is 67% (62%) when all the rainy classes are considered together, and it is respectively 65% (57%) and 65% (45%) when the C_1 and C_2 classes are considered separately.

The case studies related to 29 September 2009 (case I) at 13:00 UTC, 4 August 2010 at 14:15 UTC (case II), and 21 February 2013 at 15:00 UTC (case III) are analysed separately and the RainCEIV results are shown in Figures 3, 4, and 5 together with the C_MACSP results and the rain classes obtained from the radar-derived RR measurements. The statistical scores calculated for each case are listed in Table 12.

The case I was chosen because it highlights the RainCEIV ability in detecting very small rainy areas. On 29th September 2009 approximately at 13:00 UTC a very rapid and heavy rainfall event affected a small area between the Basilicata and Calabria regions in Southern Italy. The accuracy score is high (99%) due to the high occurrence of the non-rainy pixels detected correctly. POD shows that RainCEIV detects 67% of the rainy samples correctly, while Bias and FAR scores reveal the RainCEIV tendency to overestimate rainy samples (the FAR score is 47% and the Bias score is 1.25). In detail, the Bias score related to the C_1 class (Bias=1.37) is higher than that related to the C_2 class (Bias=1.00), on the contrary FAR related to the C_1 class (FAR=46%) is lower than that related to the C_2 class (FAR=50%). This means that there is an overestimation of the heavy rainy area but (C_1inC_2+C_0inC_2) and the number of the C_2 misses is balanced with the number of the C_2 hits. This is not true for the C_1 class that shows a higher number of hits than that of the C_2 class, and this results in a higher POD (75% and 50% for the C_1 and C_2 class respectively). In remarking this statistical results, it is worth noting that they are significantly influenced by the low number both of the C_2 RADARinSEVIRI samples (4) and C1 RADARinSEVIRI samples (8). Moreover, the temporal distance between the SEVIRI and RADAR acquisitions that is about 5 minutes can be determinant in the detection of the rainy events characterized by a high variability. It is argued that parts of the false alarms as well as the misses are brought about by the collocation errors in the SEVIRI grid.

The RainCEIV statistical scores related to cases II and III (Figures 4 and 5, respectively) are better than those related to the case study discussed above. This is because they analyse rainy events characterized by a larger temporal and spatial distribution. The case study II bears on a set of heavy and moderate rainfall events that affected Central and Southern Italy on 4th August 2010 at 14:15 UTC. RainCEIV detects rainy samples with a POD of 89% strongly related to the correct detection of the C_1 samples. In detail, POD is 82% for the C_1 class and 66% for the C_2 class resulting from the fact that the number of misses related to the C_2 class is higher than that of the C_1 class. It is important to note that 70% of the C_2 misses is misclassified as belonging to

the C_1 class. Furthermore, the number of the false alarms related to the C_1 class is higher than that of the C_2 class and this leads to a lower value both of FAR (38%) and BIAS (1.08) related to the C_2 class with respect to that related to the C_1 class (FAR=56% and BIAS=1.86). The case study III is related to the analysis of an extreme convective event characterized by very heavy precipitations occurred on 21th February 2013 on the east cost of Sicily which caused a flash flood over Catania. The RainCEIV detects all the rainy areas with a POD of 87%, that becomes 50% when only the C_2 samples are considered. The number of false alarms is higher for the C_1 class (FAR=37%) than for the C_2 class (FAR=24%), but while the C_1 samples are overestimated, RainCEIV missed the 50% of them (BIAS=0.67). It is evident that RainCEIV is missing many heavy-rainy samples, which should be due to the high temporal variability of this rainy event. Nevertheless, it is able to monitor the evolution of all the rainy areas on the east cost of Sicily and on Southern Calabria with a good approximation.

5. Conclusions

This paper proposes the RainCEIV technique as a useful tool for the continuous monitoring and characterization of the rainy areas in the Mediterranean region where there is an increased frequency of the extreme events. RainCEIV, that does not use any near real-time ancillary data, exploits the temporal differences of the brightness temperatures related to the SEVIRI water vapour channels. These are indicative of the atmosphere instability and, as a consequence, could give useful information for the detection of the rainy areas when analysed with the spectral and textural features related to the other SEVIRI channels. Because of the well-known limitations of the IR/VIS observations in determining RR values, the RainCEIV main purpose is to provide a near-real time qualitative characterization of the rainy areas especially in regions not covered by the radar and rain gauge network.

RainCEIV consists of two modules that use geostationary observations from SEVIRI in order to detect cloudy pixels and, successively, to associate them to a rainy/non-rainy class. RainCEIV uses both IR and VIS observations to determine if the SEVIRI pixel belongs to the *non-rainy* (C_0), *light-to-moderate-rainy* (C_1) or *heavy-to-very-heavy-rainy* (C_2) class. The IR/VIS observations do not have the same potentiality as MW observations in characterizing rainy areas, but their high spatial and temporal resolution are used to get a continuous monitoring of the stratiform and convective events. The RainCEIV training phase has been carried out by

collecting a set of SEVIRI pixels with co-located RR values inferred from AMSU-B/MHS observations processed by the PEMW algorithm and, when available, with co-locate radar-derived RR values. This double matching of the SEVIRI pixels is an important aspect of RainCEIV because it allows to get a reliable training dataset.

RainCEIV has been validated on the basis of the RR observations from the Italian DPC operational weather radar network. The dichotomous statistical scores indicate that a good fraction (97% for daytime validation and 96% for night-time validation) of the pixels examined are correctly identified as rainy or non-rainy by the RainCEIV. The Bias scores (1.36 for daytime validation and 1.58 for night-time validation) and the FAR scores (39% and 48%) suggest that RainCEIV tends to overestimate rainy pixels especially during the night-time, while the POD scores (81% both for daytime and night-time validation) indicate that RainCEIV detects rainy areas with a good a approximation. The rainy areas overestimation is mainly due to the misclassification of C_0 samples as C_1 samples. Moreover, the high FAR values related to the C_1 and C_2 classes are mainly due to the misclassification of the C_1 samples as C_2 samples and vice versa. The statistical scores obtained for the daytime validation are generally better than those obtained for the night-time validation. This is prevalently due to the fact that the features related to the VIS/NIR observations (unavailable during night-time) have a strong influence on the RainCEIV output because of their higher discriminatory power when compared with that of the features related to the 3.9 μm and 12.0 μm observations. In remarking upon the comparison results, it is important to bear in mind the different spatial resolutions as well as the temporal distance between radar and satellite observations that could affect the statistical scores negatively, especially for rapid convective events, even if the time distance between radar and SEVIRI acquisitions is little. As far as future developments are concerned, RainCEIV will be updated to consider in the training phase the RADARinSEVIRI samples characterized by a percentage of rainy RS samples lower than 80% so as to individuate extreme rainy events located over an area whose size is smaller than that of the SEVIRI pixel area. To this aim, information from the Visible Infrared Imaging Radiometer Suite (VIIRS) on-board the Suomi National Polar-orbiting Partnership (NPP) (characterized by higher spatial and spectral resolutions than SEVIRI) will be taken into account when available. The purpose is the integration of the SEVIRI and VIIRS observations in order to determine the cloud classification and the rainfall occurrence

probability at a better spatial resolution (from 3 km for SEVIRI to 0.375 km/0.750 km for VIIRS at the sub-satellite point).

Appendix A. "Procedure adopted for the training set refinement"

The RainCEIV and C_MACSP original training datasets have been refined by applying the same procedure to the samples of each class.

The refinement process consists in using the Nearest Neighbour decision rule described by Cover and Hart (1967) in order to classify each sample of the initial training classes. Here the aim of this process is to eliminate the redundant and misclassified training samples, which is similar to the CNN rule described in Hart (1968) but the main purpose of CNN is to get a training subset performing as well as the original one. Before the description of the refinement process, a brief description of the NN decision rule and of the Fisher criterion (used to reduce the number of the components of the feature vector) will be given.

Let $T_o=\{(\vec{x}_i, C_j)\}$ be the original training dataset, where the pairs $(\vec{\mathbf{x}}_\mathbf{i}, C_j)$ indicate the training samples $\vec{\boldsymbol{x}}_{\boldsymbol{i}}$ of the class C_j, j=1, 2, ..., N_c, N_c is the number of the classes, i=1, 2, ...,$N_{c,j}$, $N_{c,j}$is the number of the training samples for the class C_j. Given a vector $\vec{\boldsymbol{y}}$ to be the classified, the NN rule establishes that $\vec{\boldsymbol{y}}$ belongs to the class C_j when the minimum distance is that from the training sample $\vec{\boldsymbol{x}}_{\boldsymbol{i}}$ that belongs to class C_j, and then $\vec{\boldsymbol{x}}_{\boldsymbol{i}}$ is the Nearest Neighbourof $\vec{\boldsymbol{y}}$.

Before applying the RR decision rule, it is important to define the dimension of the feature vector. In fact, since the k-NN classifier performance generally decreases with the dimension of the feature vector, the number of the components (x^i) of $\vec{\mathbf{x}}$ has been reduced by applying the Fisher criterion (Ebert, 1987; Parikh, 1977) to evaluate the discriminatory power of the individual features and to choose the features characterized by the higher Fisher distance value. Let $\overline{x_j^i}$ and σ_j^i be the mean and standard deviation of the feature x^i for the training set from class C_j, thus the Fisher distance is defined as:

$$D_{ijk} = \frac{|\overline{x_j^i} - \overline{x_k^i}|}{\left(\sigma_j^i - \sigma_k^i\right)}. \quad (1)$$

It measures the ability of the feature x^i to differentiate class C_j from class C_k. The features x^j, within $\vec{\mathbf{x}}$, have been ordered in a decreasing way on the basis of the D_{ijk} values and the first d features have been chosen as the components of the feature vectors used. The dimension d has been fixed by following the suggestions in Jain and Chandrasekaran (1982), who point out that the ratio between the number of the training samples for each class and the feature vector dimension d should be at least five.

The procedure to obtain the refined training dataset, T_r, starting from the original training dataset T_o, consists in:

1. Considering the i^{th} pattern $(\vec{x}_i, C_j)$ of T_o,
2. Applying the NN decision rule and determining the following action on the basis of the three possible classification results:
   - the NN belongs to the initial belonging class C_j and the Euclidean distance is higher than zero, consequently the sample is put in T_r;
   - The NN belongs to a different class $C_i \neq C_j$, consequently the sample is reanalyzed and included in the NN class;
   - the Euclidean distance from the NN is zero, the sample is considered redundant and it is removed from T_o and not included in T_r.
3. restarting from point 2 with another sample and applying the entire process until all the training samples have been analyzed.

T_r, determined for each class is used as the definitive training dataset.

Acknowledgements

The authors acknowledge the Italian Department of Civil Protection (DPC) for providing data from the national radar network in the framework of the CETEMPS-DPC IDRA project. The staff of HIMET s.r.l is also acknowledged for greatly facilitating the access to the data archive.

References

Adler, R. F., M. J. Markus, M. J., and Fenn D. D.: Detection of severe Midwest thunderstorms using geosynchronous satellite data, Monthly Weather Review, 113, 769-781, 1985.

Adler, R. F., & Negri, A. J.: A satellite infrared technique to estimate tropical convective and stratiform rainfall, J. Appl. Meteor., 27, 30-51, 1988.

Adler, R. F., Negri, A. J., Keehn, P. R., and Hakkarinen, I. M.: Estimation of monthly rainfall over Japan and surrounding waters from a combination of low-orbit microwave and geosynchronous IR data, J. Appl. Meteor., 32, 335-356, 1993.

Ba, B. M. and Gruber, A.: GOES Multispectral Rainfall Algorithm (GMSRA), J. Appl. Meteor., 40, 1500–1514, 2001.

Babu V. S. and Viswanath, P.: Rough-fuzzy weighted k-nearest leader classifier for large data sets, Pattern Recognition, 42, 1719–1731, 2009.

Bennartz, R.: Optimal Convolution of AMSU-B to AMSU-A. J, Atmos. Oceanic Technol.,17, 1215–1225, 2000.

Bizzarri, B., Gasiewski, A. J., and Staelin, D. H.: Observing Rain by Millimetre–Submillimetre Wave Sounding From Geostationary Orbit, In: Measuring Precipitation From Space – EURAINSAT and the Future, V. Levizzani, P. Bauer, and F.J. Turk (Editors). Springer, Dordrecht, 675-692, 2007.

Capacci, D. and Porcù F.: Evaluation of a satellite multispectral VIS/IR daytime statistical rain-rate classifier and comparison with passive microwave rainfall estimates, J. Appl. Meteor. Clim., 48, 284-300, 2009.

Cimini, D., Romano F., Ricciardelli, E., Di Paola, F., Viggiano, M., Marzano, F. S., Colaiuda, V., Picciotti, E., Vulpiani, G.,and Cuomo, V.: Validation of satellite OPEMW precipitation product with ground-based weather radar and rain gauge networks, Atmos. Meas. Tech. Discuss., 6, 4279-4312, doi:10.5194/amtd-6-4279-2013, 2013.

Dasarathy, B. V.: Nearest neighbor (NN) norms: NN pattern classification techniques. B. V. Dasarathy, Ed. Los Alamitos, California: IEEE Computer Society Press, 1991.

Dasarathy, B. V.: Data mining tasks and methods: Classification Nearest-neighbor approaches. Handbook of data mining and knowledge discovery, New York: Oxford University Press, 288–298, 2002.

Di Paola, F., Casella, D., Dietrich, S., Mugnai, A., Ricciardelli, E., Romano, F., and Sanò, P.: Combined MW-IR Precipitation Evolving Technique (PET) of convective rain fields, Nat. Hazards Earth Syst. Sci., 12, 3557-3570, 2012.

Di Paola, F., Ricciardelli, E., Cimini, D., Romano, F., Viggiano, M., and Cuomo, V.: Analysis of Catania Flash Flood Case Study by Using Combined Microwave and Infrared Technique, Journal of Hydrometeorology, doi: 10.1175/JHM-D-13-092.1, in press.

Di Tomaso, E., Romano, F., and Cuomo, V.: Rainfall estimation from satellite passive microwave observations in the range 89 GHz to 190 GHz, Journal of Geophysical Research, 114, D18203, doi:10.1029/2009JD011746, 2009.

Ebert, E.: A pattern recognition technique for distinguishing surface and cloud types in the polar regions, Journal of Climate Applied Meteorology, 26, 1412-1427, 1987.

Ebert, E, (last updated 25 July, 2013): Forecast verification Issues, Methods and FAQ, 25 July 2013, (Available at http://www.cawcr.gov.au/projects/verification/), 2013.

Feidas, H. and Giannakos, A.: Classifying convective and stratiform rain using multispectral infrared Meteosat Second Generation satellite data, Theor. Appl. Climatol., 108, 613–630,2012.

Gasiewski, A. J., Voronovich, A., Weber, B. L., Stankov, B., Klein, M., Hill, R. J.; and Bao, J.W.: Geosynchronous microwave (GEM) sounder/imager observation system simulation, Geoscience and Remote Sensing Symposium, 2003. IGARSS '03. Proceedings. 2003 IEEE International, 2, 1209-1211, 21-25 July 2003, 2003.

Hamamoto, Y., Uchimura, S., and Tomita S.: A Bootstrap Technique for Nearest Neighbor Classifier Design, IEEE transaction on pattern analysis and machine intelligence, 19, 73-79, 1997.

Hart, P. E.: The Condensed Nearest Neighbor Rule, IEEE Transactions on Information Theory, 14, 3, 515-516, 1968.

Heinemann, T., Lattanzio, A., and Roveda, F.: The Eumetsat multi-sensor precipitation estimate (MPE), In Second International Precipitation Working group (IPWG) Meeting, Madrid, Spain, September, 2002.

Hsu, K., Gao, X., Sorooshian, S., and Gupta, H. V.: Precipitation estimation from remotely sensed information using artificial neural networks, J. Appl. Meteorol. , 36, 1176–1190, 1997.

Jain, A. K. and Chandrasekaran, B.: Dimensionality and sample size considerations in pattern recognition practice. In: Krishnaiah, P.R., Kanal, L.N. (Eds.), Handbook of Statistics, 2. North-Holland Publishing Company, 835–855, 1982.

Jobard, I. and Desbois, M.: Satellite estimation of the tropical precipitation using the Meteosat and SSM/I data, Atmospheric Research, 34, 285-298, 1994.

Joyce, R. J., Janowiak, J. E., Arkin, P. A., and Xie, P.: CMORPH: a method that produces global precipitation estimates from passive microwave and infrared data at high spatial and temporal resolutions, J. Hydrometeorol., 5, 487–503, 2004.

Kidd, C., Kniveton, D. R., Todd, M. C., and Bellerby, T. J.: Satellite rainfall estimation using a combined passive microwave and infrared algorithm, J. Hydrometeorol., 4, 1088–1104, 2003.

Kidd, C. and Levizzani, V.: Status of satellite precipitation retrievals. Hydrology and Earth System Sciences, 15, 1109-1116. doi: **http://dx.doi.org/10.5194/hess-15-1109-2011,** 2011.

Kühnlein, M., Thies, B., Nauß, T., and Bendix, J.: Rainfall-Rate Assignment Using MSG SEVIRI Data-A Promising Approach to Spaceborne Rainfall-Rate Retrieval for Midlatitudes, J. Appl. Meteor. Climatol., 49, 1477–1495, 2011.

Lambrigtsen, B.; Tanner, A.; Gaier, T.; Kangaslahti, P.; and Brown, S.: A Microwave Sounder for GOES-R Developing the GeoSTAR Mission. Geoscience and Remote Sensing Symposium, 2006. IGARSS 2006, IEEE International Conference, 3964-3967, July 31 2006-Aug, 2006.

Lensky, I. M. and Rosenfeld, D.: Estimation of Precipitation Area and Rain Intensity Based on the Microphysical Properties Retrieved from NOAA AVHRR Data, J. Appl. Meteor. Climatol., 36, 234-242, 1997.

Lensky, I. M. and Rosenfeld, D.: Clouds-Aerosols-Precipitation Satellite Analysis Tool (CAPSAT), Atmos. Chem. Phys., 8, 6739-6753, 2008.

Marzano, F. S., Palmacci, M., Cimini, D., Giuliani, G. and Turk, J. F.: Multivariate Statistical Integration of Satellite Infrared and Microwave Radiometric Measurements for Rainfall Retrieval at the Geostationary Scale, IEEE Trans. Geosci. Remote Sens., 42, 5, 1018-1032,2004.

Mosher, F. R.: A satellite diagnostic of global convection, Preprints, 11th Conference on Satellite Meteorology, 416-419, 2001.

Mosher, F. R.: Detection of deep convection around the globe, Preprints, 10th Conference on Aviation, Range and Aerospace Meteorology, Madison, WI, American Meteorological Society, 416-419, 2001.

Mugnai, A., Casella, D., Cattani, E., Dietrich, S., Laviola, S., Levizzani, V., Panegrossi, G., Petracca, M., Sanò, P., Di Paola, F. et al.: Precipitation Product from the hydrology SAF, Nat. Hazards Earth Syst. Sci., 13, 1959-1981, 2013.

Negri, A. J. and Adler, R. F.: Relation of satellite based thunderstorm intensity to radar estimated rainfall, J. Appl. Meteor., 20, 288-300, 1981.

Parikh, J.: A comparative Study of Cloud classification Techniques, Remote Sensing of Environment, 6, 67–81, 1977.

Puca, S., Porcu, F., Rinollo, A., Vulpiani, G., Baguis, P., Balabanova, S., Campione, E., Ertürk, A., Gabellani, S., Iwanski, R., Jurašek, M., Kanák, J., Kerényi, J., Koshinchanov, G., Kozinarova, G., Krahe, P., Lapeta, B., Lábó, E., Milani, L., Okon, L'., Öztopal, A., Pagliara, P., Pignone, F., Rachimow, C., Rebora, N., Roulin, E., Sönmez, I., Toniazzo, A., Biron, D., Casella, D., Cattani, E., Dietrich, S., Di Paola, F., Laviola, S., Levizzani, V., Melfi, D., Mugnai, A., Panegrossi, G., Petracca, M., Sanò, P., Zauli, F., Rosci, P., De Leonibus, L., Agosta, E., and Gattari, F.: The validation service of the hydrological SAF geostationary and polar satellite precipitation products, Nat. Hazards Earth Syst. Sci., 14, 871-889, doi:10.5194/nhess-14-871-2014, 2014.

Ricciardelli, E., Romano, F., and Cuomo, V.: Physical and statistical approaches for cloud identification using Meteosat Second Generation – Spinning Enhanced Visibile and Infrared Imager, Remote Sensing of Environment, 112, 2741-2760, 2008.

Rinollo, A., Vulpiani, G., Puca, S., Pagliara, P., Kanák, J., Lábó, E., Okon, L'., Roulin, E., Baguis, P., Cattani, E., Laviola, S., and Levizzani, V.: Definition and impact of a quality index

for radar-based reference measurements in the H-SAF precipitation product validation, Nat. Hazards Earth Syst. Sci., 13, 2695-2705, doi:10.5194/nhess-13-2695-2013, 2013.

Schmetz, J., Pili, P., Tjemkes, S., Just, D., Kermann, J., Rota, S., et al.: An introduction to Meteosat Second Generation (MSG), Bull. Amer. Meteor. Soc, 977−992, 2002.

Scofield, R. A.: The NESDIS operational convective precipitation technique, Mon. Wea. Rev., 115, 1773-1792, 1987.

Turk, J. F., Rohaly, G., Hawkins, J., Smith, E. A., Marzano, F. S., Mugnai, A., and Levizzani, V.: Meteorological applications of precipitation estimation from combined SSM/I, TRMM, and geostationary satellite data. in Microwave Radiometry and Remote Sensing of the Environment, P. Pampaloni Ed., VSP Intern. Sci. Publisher, Utrecht (NL), 353-363, 2000.

Vicente, G. A., Menzel W. P., and Scofield, R. A.: The Operational GOES Infrared Rainfall Estimation Technique, Bull. Amer. Meteor. Soc., 79, 1883–1898, 1998.

Viswanath, P. and Sarma, H.: An Improvement to k-Nearest Neighbor Classifier, Recent Advances in Intelligent Computational Systems, 227-231, ISBN: 978-1-4244-9478-1, 2011.

Vulpiani, G., Pagliara, P., Negri, M., Rossi, L., Gioia, A., Giordano, P., Alberoni, P. P., Cremonini, R., Ferraris, L., and Marzano, F. S.: The Italian radar network within the national early-warning system for multi-risks management, Proc. of Fifth European Conference on Radar in Meteorology and Hydrology (ERAD 2008), 184, Finnish Meteorological Institute, Helsinki, 30 June - 4 July, 2008.

Vulpiani, G., Montopoli, M., Delli Passeri, L., Gioia, A. G., Giordano, P., Marzano, F. S.: On the Use of Dual-Polarized C-Band Radar for Operational Rainfall Retrieval in Mountainous Areas. J. Appl. Meteor. Climatol., 51, 405–425. doi:10.1175/JAMC-D-10-05024.1, 2012.

Wu R., Weinman J. A., and Chin, R. T.: Determination of Rainfall Rates from GOES Satellite Images by a Pattern Recognition Technique, J. Atmos. Oceanic Technol., 2, 314–330, 1985.

Table 1. List of the NOAA satellite overpasses for the AMSU-B PEMW rain rate maps considered in the training phase

Date	NOAA satellite overpass time (UTC) over Mediterranean area
29 September 2009	15:16, 17:22
1 October 2009	04:37, 05:13, 08:30, 13:03, 15:56, 16:37, 19:18
2 October 2009	01:25, 04:13
4 March 2010	14:23, 16:03, 16:28, 20:05
5 March 2010	00:56, 01:48, 04:16, 06:24, 08:20, 11:40
26 April 2010	12:47, 13:20, 14:49
28 april 2010	12:26, 15:45
2 May 2010	15:45, 16:32, 19:44
20 June 2010	11:42, 11:58, 14:28
21 June 2010	02:00
23 June 2010	12:52
4 August 2010	10:43, 12:19, 16:24, 18:03, 18:56, 20:38
4 October 2010	03:54, 06:15, 10:16, 13:14, 15:17, 17:44, 19:33
1 March 2011	11:22, 8:48, 20:15
12 February 2012	01:08, 01:38
21 February 2013	11:20, 13:10
7 October 2013	09:14, 14:38, 20:38
8 October 2013	08:55, 12:10, 14:30, 20:18, 20:25
9 October 2013	08:32, 11:56, 19:56
10 October 2013	08:12, 09:52, 19:35
17 November 2013	08:25, 10:06, 11:36, 13:17, 19:48
18 November 2013	08:05, 09:45, 11:25,13:06
1 December 2013	08:00, 08:36, 20:00
2 December 2013	07:50, 08:15, 09:55, 19:38
3 December 2013	09:35, 12:03, 19:16, 21:00

Table 2. Statistical scores related to the RainCEIV rain rate results obtained classifying the initial and artificial test dataset for k=3. The statistical scores are shown for all the rainy classes (C_1, C_2), light to moderate rain (C_1), and heavy to very heavy rain (C_2).

	Test dataset	C_1, C_2	C_1	C_2	C_1, C_2	C_1	C_2	C_1, C_2	C_1	C_2
		k=3, d=10			k=3, d=16			k=3,d=20		
Accuracy	Artificial	0.72	0.75	0.76	0.81	0.78	0.79	0.81	0.77	0.78
	Initial	0.81	0.81	0.82	0.80	0.76	0.81	0.77	0.74	0.81
Bias	Artificial	0.96	0.99	0.94	1.01	1.02	1.00	1.01	1.01	1.00
	Initial	0.98	0.92	1.04	0.99	1.05	0.92	0.97	1.02	0.92
POD	Artificial	0.77	0.63	0.62	0.86	0.68	0.68	0.86	0.66	0.67
	Initial	0.85	0.69	0.74	0.84	0.68	0.68	0.82	0.63	0.68
HSS	Artificial	0.37	0.44	0.46	0.56	0.50	0.52	0.56	0.48	0.50
	Initial	0.57	0.57	0.59	0.55	0.47	0.57	0.50	0.42	0.57
FAR	Artificial	0.20	0.37	0.34	0.15	0.34	0.32	0.14	0.35	0.33
	Initial	0.13	0.25	0.29	0.14	0.36	0.26	0.16	0.39	0.26

Table 3. Statistical scores related to the RainCEIV rain rate results obtained classifying the initial and artificial test dataset for k=5. The statistical scores are shown for all the rainy classes (C_1, C_2), light to moderate rain (C_1), and heavy to very heavy rain (C_2).

	Test dataset	C_1, C_2	C_1	C_2	C_1, C_2	C_1	C_2	C_1, C_2	C_1	C_2
		k=5, d=10			k=5, d=16			k=5, d=20		
Accuracy	Artificial	0.73	0.76	0.76	0.85	0.79	0.82	0.85	0.79	0.81
	Initial	0.81	0.82	0.84	0.86	0.81	0.85	0.85	0.79	0.84
Bias	Artificial	0.96	0.98	0.94	0.99	1.00	0.98	0.99	1.01	0.97
	Initial	0.97	0.94	0.99	1.00	1.11	0.90	1.00	1.10	0.90
POD	Artificial	0.77	0.64	0.62	0.89	0.70	0.72	0.88	0.68	0.69
	Initial	0.84	0.70	0.74	0.90	0.76	0.74	0.89	0.73	0.72
HSS	Artificial	0.40	0.47	0.46	0.67	0.55	0.59	0.66	0.52	0.56
	Initial	0.59	0.58	0.62	0.68	0.58	0.66	0.67	0.54	0.64
FAR	Artificial	0.19	0.35	0.34	0.11	0.30	0.26	0.11	0.32	0.28
	Initial	0.13	0.25	0.25	0.10	0.31	0.18	0.11	0.33	0.20

Table 4. Statistical scores related to the RainCEIV rain rate results in classifying the initial and artificial test dataset for k=7. The statistical scores are shown for all the rainy classes (C_1, C_2), light to moderate rain (C_1), and heavy to very heavy rain (C_2).

	Test dataset	C_1, C_2	C_1	C_2	C_1, C_2	C_1	C_2	C_1, C_2	C_1	C_2
		k=7, d=10			k=7, d=16			k=7,d=20		
Accuracy	Artificial	0.72	0.76	0.77	0.83	0.77	0.81	0.82	0.76	0.81
	Initial	0.78	0.77	0.80	0.80	0.78	0.81	0.80	0.78	0.81
Bias	Artificial	0.97	1.05	0.94	1.00	1.02	0.98	1.00	1.02	0.97
	Initial	1.00	0.94	0.95	1.01	1.09	0.93	1.01	1.09	0.93
POD	Artificial	0.78	0.64	0.62	0.87	0.67	0.71	0.87	0.66	0.71
	Initial	0.83	0.68	0.68	0.86	0.72	0.68	0.86	0.72	0.68
HSS	Artificial	0.38	0.46	0.34	0.62	0.50	0.58	0.61	0.48	0.57
	Initial	0.50	0.48	0.55	0.55	0.52	0.57	0.55	0.52	0.57
FAR	Artificial	0.20	0.36	0.46	0.12	0.34	0.27	0.12	0.35	0.28
	Initial	0.16	0.36	0.29	0.16	0.34	0.26	0.16	0.34	0.26

Table 5. Summary of the features considered for use in the RainCEIV k-NNM classifier during daytime. Label "A" means that the feature is used for all the C-MACSP classes; "LM" means that the feature is used for the low/middle cloud class; **"**HT/C" means that the feature is used for the high thick and convective cloud class.

Features	MSG-SEVIRI spectral bands (μm)							
	VIS 0.6	VIS 0.8	NIR 1.6	IR 3.9	IR 6.2	IR 7.3	IR 10.8	IR 12.0
Max Gray level							A	
Min Gray level							A	
Mean Gray level	A							
Max/Min(Gray level)								
Max(Contrast 0^o, 45^o, 90^o, 135^o)							A	
Max(Entropy 0^o, 45^o, 90^o, 135^o)			A					
Max (Mean 0^o, 45^o, 90^o, 135^o)			A			A		
Max (ASM 0^o, 45^o, 90^o, 135^o)		A		LM				
Min(Contrast 0^o, 45^o, 90^o, 135^o)								
Min(Entropy 0^o, 45^o, 90^o, 135^o)							A	
Min (Mean 0^o, 45^o, 90^o, 135^o)					A			A
Min (ASM 0^o, 45^o, 90^o, 135^o)								A
ΔTB_{15-30}					A	HT/C		
ΔTB_{15-45}					A	A		
ΔTB_{30-45}								

Table 6. Summary of the features considered for use in the RainCEIV k-NNM classifier during night-time. Label "A" means that the feature is used for all the C-MACSP classes; "LM" means that the feature is used for the low/middle cloud class; **"**HT/C" means that the feature is used for the high thick and convective cloud class.

Features	MSG-SEVIRI spectral bands (μm)				
	IR 3.9	IR 6.2	IR 7.3	IR 10.8	IR 12.0
Max Gray level				A	
Min Gray level	A			A	
Mean Gray level					
Max/Min(Gray level)					
Max(Contrast 0^o, 45^o, 90^o, 135^o)				A	
Max(Entropy 0^o, 45^o, 90^o, 135^o)	A				
Max (Mean 0^o, 45^o, 90^o, 135^o)			A	LM	
Max (ASM 0^o, 45^o, 90^o, 135^o)	LM				
Min(Contrast 0^o, 45^o, 90^o, 135^o)					HT/C
Min(Entropy 0^o, 45^o, 90^o, 135^o)				A	
Min (Mean 0^o, 45^o, 90^o, 135^o)		A			A
Min (ASM 0^o, 45^o, 90^o, 135^o)					A
ΔTB_{15-30}		A	HT/C		
ΔTB_{15-45}		A	A		
ΔTB_{30-45}			A		

Table 7. Accuracy of the C_MACSP algorithm on an independent dataset

Classes	Classification accuracy (for test samples acquired during daytime)	Classification accuracy (for test dataset acquired during nighttime)
Clear over land	95.0 %	95.0 %
Clear over sea	96.7 %	96.7 %
Low/middle clouds over land	91.6 %	91.0 %
Low/middle clouds over sea	92.6 %	91.3 %
High thin clouds over land	85.0 %	84.0 %
High thin clouds over sea	87.6 %	87.6 %
High thick clouds over land	98.3 %	97.3 %
High thick clouds over sea	99.0 %	99.0 %
Convective clouds over land	96.0 %	96.7 %
Convective clouds over sea	96.7 %	96.7 %

Table 8. List of case studies used for validation.

Date	Radar Measurement time (UTC)	Satellite overpass time (UTC) over Mediterranean region
2 May 2009	15:00, 12:30	14:55, 12:25
19 September 2009	09:00, 19:15, 19:30	08:55, 19:10, 19:25
29 September 2009	13:00 (case I), 13:15	12:55, 13:10
8 January 2010	11:00, 13:00, 16:30	10:55, 12:55, 16:25
9 March 2010	17:00	16:55
23 June 2010	15:00	14:55
1 July 2010	16:45	16:40
6 July 2010	11:30, 12:30	11:25, 12:25
4 August 2010	13:00, 13:15,14:15 (case II)	12:55, 13:10, 14:10
21 February 2013	14:30, 15:00 (case III), 15:30	14:55, 14:25, 15:25
7 October 2013	01:00, 03:00, 02:00	00:55, 02:55, 01,55
8 October 2013	12:00, 19:00	11:55, 18:55
25 December 2013	07:00	06:55
18 January 2014	06:00, 18:00, 20:00	05:55, 17:55, 19:55

1 Table 9**.** Contingency table for the dichotomous statistical assessment of the RainCEIV
2 algorithm for all the pixels used for daytime validation.

		Radar- derived rain rate results		
RainCEIV results		Yes	no	marginal total
	yes	18,410	12,264	30,674
	no	4,052	536,124	540,176
	marginal total	22,462	548,388	570,850

3 8

4

Table 10**.** Contingency table for the dichotomous statistical assessment of the RainCEIV algorithm for all the pixels used for night-time validation.

		Radar- derived rain rate results		
RainCEIV results		Yes	no	marginal total
	yes	16,399	15,295	31,694
	no	3,604	470,486	474,090
	marginal total	20,003	485,781	505,784

Table 11**.** Dichotomous Statistical scores (RainCEIV versus radar-derived rain rate measurements) for the case studies listed in Table 8. The statistical scores are shown for all rainy classes (C_1, C_2), light to moderate rain (C_1), and heavy to very heavy rain (C_2).

Statistical Scores	for daytime validation dataset			for night-time validation dataset		
	C_1, C_2	C_1	C_2	C_1, C_2	C_1	C_2
Accuracy	0.97	0.97	0.99	0.96	0.96	0.99
Bias	1.36	1.33	1.65	1.58	1.55	1.89
POD	0.81	0.77	0.86	0.81	0.75	0.65
HSS	0.67	0.65	0.65	0.62	0.57	0.45
FAR	0.39	0.41	0.47	0.48	0.51	0.65

Table 12. Dichotomous statistical scores shown for all rainy classes (C_1, C_2), light to moderate rain (C_1), and heavy to very heavy rain (C_2), for the case studies I, II and III.

Statistical score	Case I 29 September 2009, 13:00 UTC			Case II 4 August 2010, 14:15 UTC			Case III 21 February 2013, 15:00 UTC		
	C_1, C_2	C_1	C_2	C_1, C_2	C_1	C_2	C_1, C_2	C_1	C_2
Accuracy	0.99	0.99	0.99	0.99	0.98	0.99	0.92	0.92	0.99
Bias score	1.25	1.38	1.00	1.56	1.86	1.08	1.35	1.38	0.67
POD	0.67	0.75	0.50	0.89	0.82	0.66	0.87	0.87	0.50
HSS	0.59	0.63	0.50	0.68	0.56	0.63	0.70	0.68	0.60
FAR	0.47	0.45	0.50	0.43	0.56	0.38	0.35	0.37	0.24

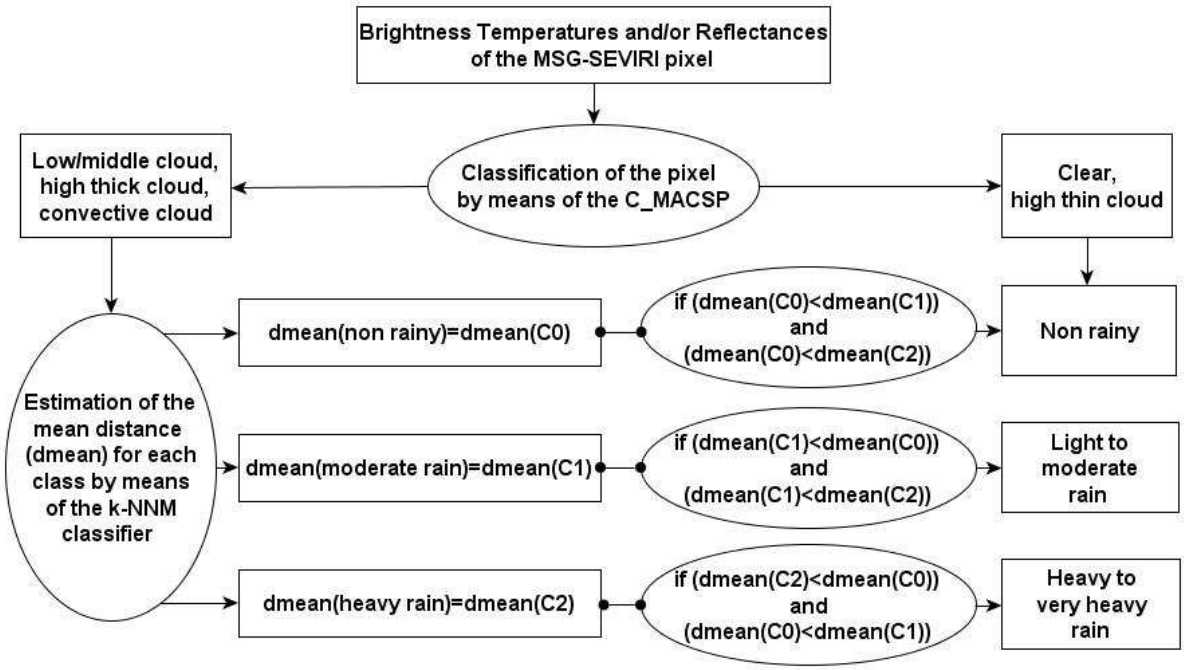

Figure 1. Flowchart of the RainCEIV algorithm.

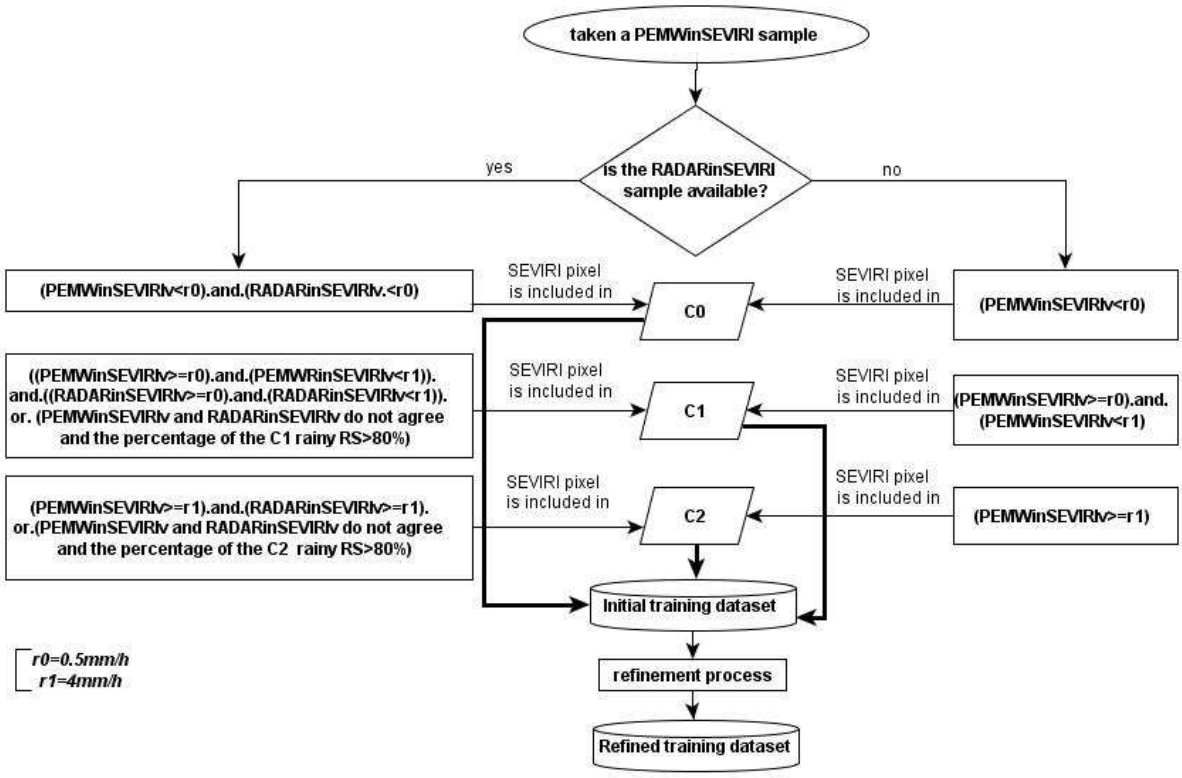

Figure 2 Flowchart of the RainCEIV training procedure.

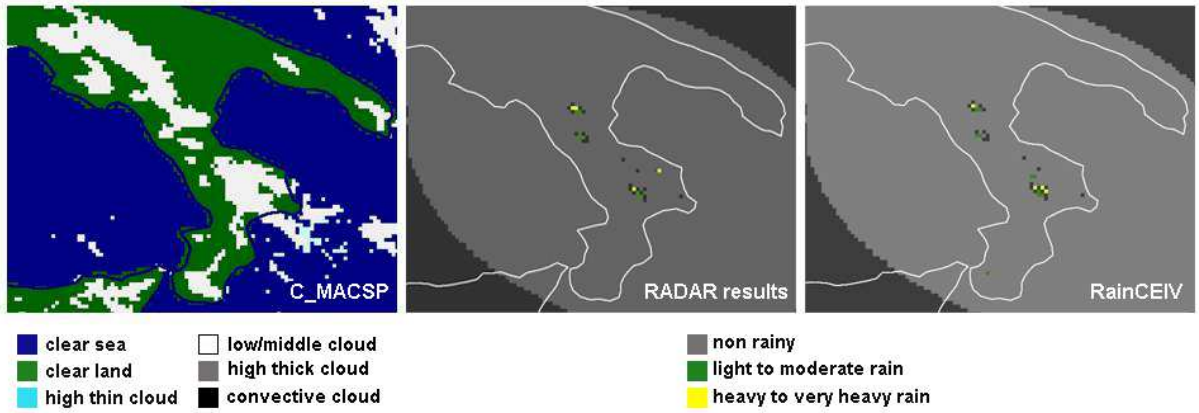

Figure 3. 29 September 2009 at 13:00 UTC. From left to right: C_MACSP cloud classification results, radar-derived rain rate results, RainCEIV rain rate results.

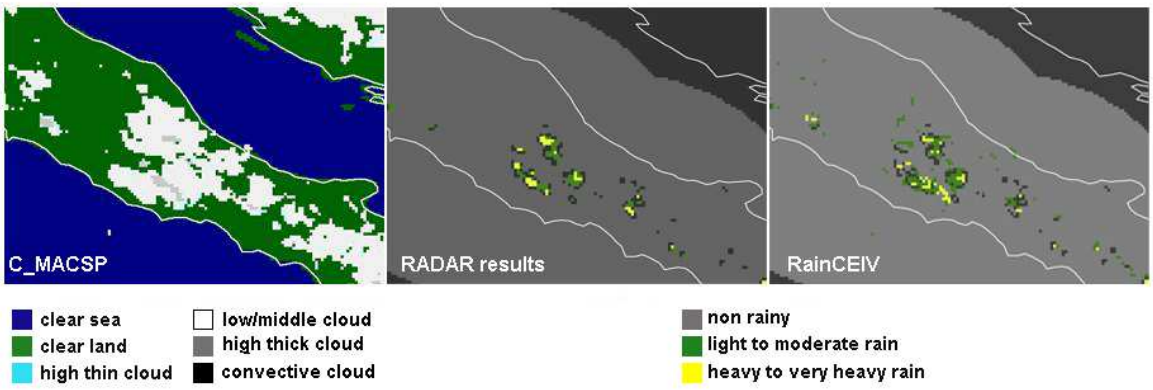

Figure 4. 4 August 2010 at 14:15 UTC. From left to right: C_MACSP cloud classification results, radar-derived rain rate results, RainCEIV rain rate results.

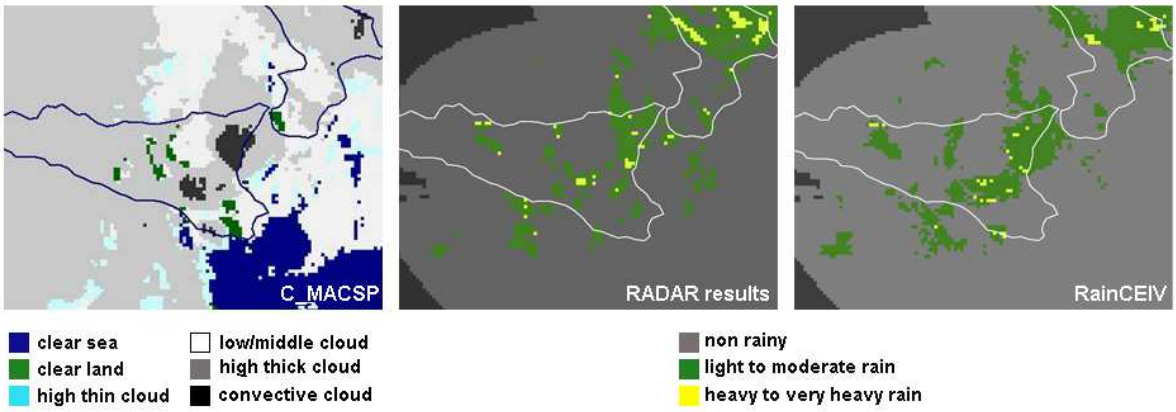

Figure 5. 21 February 2013 at 15:00 UTC. From left to right: C_MACSP cloud classification results, radar-derived rain rate results, RainCEIV rain rate results.